PHYSICAL REVIEW E **90**, 051102(R) (2014)

Kinetic effects and nonlinear heating in intense x-ray-laser-produced carbon plasmas

Y. Sentoku, I. Paraschiv, R. Royle, and R. C. Mancini
Department of Physics, University of Nevada, Reno, Nevada 89557, USA

T. Johzaki
Graduate School of Engineering, Hiroshima University, Hiroshima Prefecture 739-8527, Japan

(Received 20 May 2014; published 21 November 2014)

The x-ray laser-matter interaction for a low-Z material, carbon, is studied with a particle-in-cell code that solves the photoionization and x-ray transport self-consistently. Photoionization is the dominant absorption mechanism and nonthermal photoelectrons are produced with energy near the x-ray photon energy. The photoelectrons ionize the target rapidly via collisional impact ionization and field ionization, producing a hot plasma column behind the laser pulse. The radial size of the heated region becomes larger than the laser spot size due to the kinetic nature of the photoelectrons. The plasma can have a temperature of more than 10 000 K (>1 eV), an energy density greater than 10^4 J/cm^3, an ion-ion Coulomb coupling parameter $\Gamma \geqslant 1$, and electron degeneracy $\Theta \geqslant 1$, i.e., strongly coupled warm dense matter. By increasing the laser intensity, the plasma temperature rises nonlinearly from tens of eV to hundreds of eV, bringing it into the high energy density matter regime. The heating depth and temperature are also controllable by changing the photon energy of the incident laser light.

DOI: 10.1103/PhysRevE.90.051102 PACS number(s): 52.65.Rr, 52.50.Jm

The high-intensity x-ray free-electron lasers (XFELs) that are now available, such as the LCLS (Stanford, USA) [1], SACLA (Japan) [2], and soon the European XFEL (Germany) [3], are becoming an attractive way of producing hot dense plasmas. The energy delivered by the XFELs is around a millijoule, with more than 10^{12} photons in less than 100 fs. The photon energy is tunable from a few keV to 20 keV. By tightly focusing the beam to a micron-scale spot, an XFEL on-target intensity can reach more than 10^{18} W/cm^2. The advantage of using an x-ray laser for isochoric heating is that it can penetrate deeply into solid matter and heat it directly to more than 10^6 K ($\sim$100 eV) [4]. Such extreme states of matter are of considerable interest due to their relevance to astrophysical plasmas found in stellar interiors, giant planet cores [5], galactic nuclei, and x-ray binaries [6]. Additionally, they will allow novel ways of studying equation-of-state and opacity physics under Gbar pressure and strong fields.

Since the x-ray laser-matter interaction occurs in such a short time ($\ll$1 ps), thermalization or equilibrium cannot be assumed and we must treat the plasma kinetically. We have developed a simulation tool based on the two-dimensional (2D) collisional particle-in-cell (PIC) code, PICLS [7], in which we now solve the x-ray transport and photoionization self-consistently with the plasma dynamics.

The following radiation transport equation is solved,

$$\left(\frac{1}{c}\frac{\partial}{\partial t} + \mathbf{n}\cdot\nabla\right) I = \eta - \chi I, \tag{1}$$

where $I(\mathbf{r},\Omega,\nu,t)$, $\eta(\mathbf{r},\nu,t)$, $\chi(\mathbf{r},\nu,t)$, $\Omega(\theta,\phi)$, c, and ν are the spectral radiation intensity (J/cm^2/Hz/sr), emissivity (J/cm^3/s/Hz/sr), opacity (1/cm), solid angle (sr), speed of light, and x-ray frequency, respectively. The unit vector $\mathbf{n}$ is along the ray direction and is expressed as $(\cos\theta, \sin\theta\cos\phi, \sin\theta\sin\phi)$ in polar coordinates. The x-ray photons are grouped nonuniformly by photon energy ($h\nu$), and the groups are adaptively selected to capture the characteristic bound-bound and bound-free transitions. The spectral intensity I for each photon group is discretized in a solid angle Ω by the discrete ordinate method [8] and is solved in each direction explicitly using the constrained interpolation profile (CIP) scheme [9]. A database of nonlocal thermodynamical equilibrium (non-LTE) η and χ as a function of temperature, density, and photon energy is precalculated with the FLYCHK code [10] and used by PICLS to characterize the material's radiative properties during the simulation. The PIC code calculates the plasma parameters (electron density n_e and bulk electron temperature T_e) which are used by the radiation transport module to calculate η and χ by interpolation in the database. The energy transfer between the plasma and x rays is calculated self-consistently, i.e., the plasma loses (gains) thermal energy at the location where the x rays are emitted (absorbed).

We have also developed a photoionization model based on Kramers' cross section formula [11]. For each ionization state, we model the total photoionization cross section by adding up the contributions from all occupied shells, namely,

$$\sigma_{\rm pi} = \kappa \sum_n \frac{64\pi\alpha a_0^2}{3\sqrt{3}} \frac{\omega_n n}{(Z_i+1)^2} \left(\frac{I_n}{h\nu}\right)^3, \tag{2}$$

where $h\nu$, α, ω_n, n, I_n, and Z_i are the photon energy, fine-structure constant, number of bound electrons in the n shell, principal quantum number, ionization energy, and ionization degree, respectively. Here κ is a parameter to adjust the cross section to that of cold matter [12]. This is a simplified model for a single photon process suitable for inline evaluation in a PIC code that still captures the main characteristics of the photoionization process. With the local photon energy density n_ν calculated by the radiation transport module, the photoionization probability per unit of time is evaluated as $\sigma_{\rm pi} n_\nu c$. The ionizations are then performed randomly by a Monte Carlo scheme for each ion and each radiation transport time step, similar to the collisional ionization [13]. When a photoionization occurs, the photon is annihilated and its energy is given to a newly created photoelectron after

subtracting the ionization energy I_p required to ionize from Z_i to $Z_i + 1$, so that the photoelectron's initial energy is given by $\epsilon_{\rm pe} = h\nu - I_p$. Its direction is produced randomly in 4π sr. In reality, photoelectrons are produced with specific angular distributions [14]. However, since they are rapidly thermalized by collisions, the results presented here are not sensitive to the details of their initial direction of motion. This was confirmed by doing simulations for several cases of angular distribution, including isotropic and unidirectional.

We apply the code to the intense x-ray laser-matter interaction. The target is solid graphite with a mass density $\rho = 2.3\ {\rm g/cm^3}$ so that the ion density is $n_i = 1.1 \times 10^{23}\ {\rm cm^{-3}}$. Initially the target is neutral with $Z_i = 0$. The x-ray laser, incident from the left boundary, is monochromatic with 9 keV photons and has an intensity of $10^{18}\ {\rm W/cm^2}$ and an energy of about 2 mJ. It has a constant temporal profile with a duration $\tau = 60$ fs and is focused in a Gaussian spot with a radius $r_0 = 1\ \mu$m half width at half maximum. We used 130 photon energy groups adaptively selected in a range of 1 eV to 10 keV. The 2π solid angle for the upper hemisphere is discretized into 146 directions, while the lower hemisphere is assumed symmetric. The PIC simulation uses 1700×2560 cells for a $34 \times 52\ \mu$m system box. The target is 30 μm thick with a 4 μm vacuum zone in front. The radiation transport cell size is 10×10 times larger than the PIC cell size, and the radiation transport calculation is performed once every ten PIC time steps.

The simulation includes Coulomb collisions for partially ionized plasmas, and electron collisional impact ionizations [13]. The plasma collision frequency [15] is used except when the plasma temperature is less than the Fermi energy (~10 eV for solid graphite), in which case we use the collision frequency for a degenerate plasma to avoid a divergence [7]. Recombination is not included in the current simulation. The three-body recombination rate for $n = 2$ level electrons in solid carbon is negligible when the plasma temperature $T > 0.5$ eV and is only comparable to the impact ionization rate for $n = 1$ electrons when $T < 5$ eV.

Figure 1 shows the simulation results. The x-ray laser easily penetrates the solid carbon and is only slightly attenuated at the pulse front, as seen in Fig. 1(a). The cold opacity $\chi_{\rm pi} = \sigma_{\rm pi} n_i$ caused by photoionization for neutral carbon is about 7 ${\rm cm^{-1}}$ for 9 keV photons [12]—namely, the laser can penetrate solid graphite more than a millimeter. As ionizations proceed, the photoionization cross section becomes smaller by a factor of $1/(Z_i + 1)$ and also due to the reduction in the number of bound electrons available for ionization, and thus the penetration depth is longer than that estimated by the cold carbon opacity. Note that other opacity contributions are smaller than that of photoionization for the plasma conditions discussed here, so that the dominant absorption process for 9 keV photons in a carbon target is photoionization, though we include all processes in the simulation. Another absorption process to consider is Compton scattering, however, for $h\nu < 10$ keV in carbon it is a small effect since the cross section is an order of magnitude smaller than that of photoionization.

The formation of a stable, hot plasma column is observed after the pulse has passed through the target, as seen in Fig. 1(b). The average charge state at the center is $Z_i \sim 0.5$,

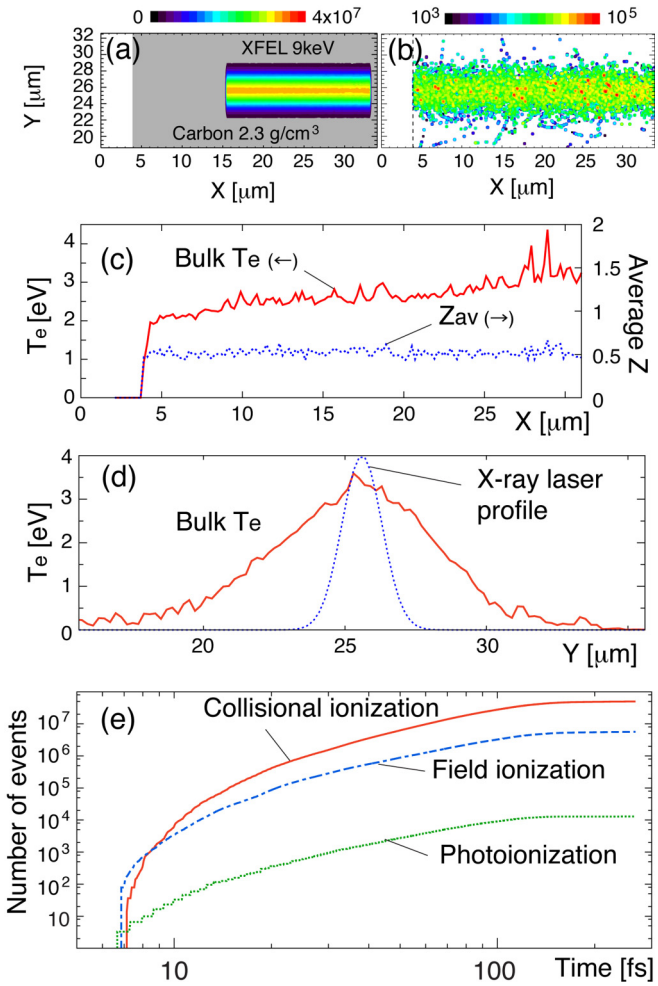

FIG. 1. (Color online) 2D PICLS simulation results for (a) the x-ray laser energy density (J/cm^3) (linear scale) at 110 fs, and (b) the electron energy density (J/cm^3) (logarithmic scale) at 200 fs. (c) Bulk electron temperature (red solid line) and average charge state (blue dotted line) along the laser axis at 200 fs. (d) Transverse profile of the bulk electron temperature at 200 fs averaged from $X = 10$ to 30 μm. (e) Time evolution of the total number of ionization events in the system.

as seen in Fig. 1(c), and the hot region is localized around the pulse path. About 2% of the laser energy is lost after passing though 30 μm. The temperature averaged along the central axis is ~3 eV, which is much smaller than the temperature we would expect from the absorbed energy. It was found that the temperature remains low because ~80% of the absorbed energy is spent in collisional ionizations, as discussed below. The energy density at the center is $\sim 3 \times 10^4\ {\rm J/cm^3}$, which is in the regime of high energy density matter.

Next, the stopping range and time scale of relaxation of the photoelectrons are estimated. The photoelectron energy is $\epsilon_{\rm pe} \sim 9$ keV in low-Z material since the ionization energy is much smaller than the photon energy. Then the photoelectron stopping power in solid carbon is ~20 MeV cm^2/g from the NIST database [16], giving a stopping range of ~2 μm. Also, by solving the energy transfer equation for the photoelectrons and the bulk electrons using the plasma collision frequency,

we find the relaxation time scale to be ∼50 fs, during which time a photoelectron can move a few microns, consistent with the stopping range. The kinetic processes occurring before thermalization are important in determining the extent of the heated region, which becomes several microns wider than the laser spot size, as seen in Fig. 1(d).

The time evolution of the number of ionization events [Fig. 1(e)] shows that collisional ionization, initiated by photoelectrons as well as secondary hot thermal electrons, is the the dominant ionization process. Although photoionization is minor, it provides the photoelectrons responsible for initiating the heating processes. The field ionization driven by the charge separation due to the collective effect of the fast photoelectrons is also important, especially at the pulse front and at the edge of heated region.

Using the cold photoionization opacity $\chi_{\rm pi}$, we can estimate the energy deposition by the photoelectrons. The photoionization rate $\chi_{\rm pi} n_\nu c$ results in a photoelectron number density $n_{\rm pe} = \chi_{\rm pi} n_\nu c\tau \sim 3 \times 10^{20}$ cm^{-3}, where the photon number density is $n_\nu = I/c\,h\nu \sim 2.3 \times 10^{22}$ cm^{-3}. However, the $n_{\rm pe}$ observed along the laser axis in a simulation without impact and field ionization is about 30% of this value. The smaller than expected density is due to an overestimation of $\chi_{\rm pi}$ using the cold opacity. By averaging the total photoelectron energy among the electrons in the plasma column with charge state $Z_i \sim 0.5$, the bulk electron temperature is ∼15 eV, which is close to the temperature we observed in the simulation without the ionizations. As previously mentioned, about 80% of the absorbed energy is taken by impact ionizations, reducing the plasma temperature to about 3 eV, which agrees with the results shown in Fig. 1.

Next, we study the scaling of various parameters with respect to laser intensity in the range of 3×10^{17}–3×10^{20} W/cm^2, keeping all other parameters fixed. Figure 2 shows the intensity dependence of the absorption, electron temperature, average Z, and ratio of collisional ionization energy to absorbed energy. The absorption decreases and the average charge state increases with increasing laser intensity.

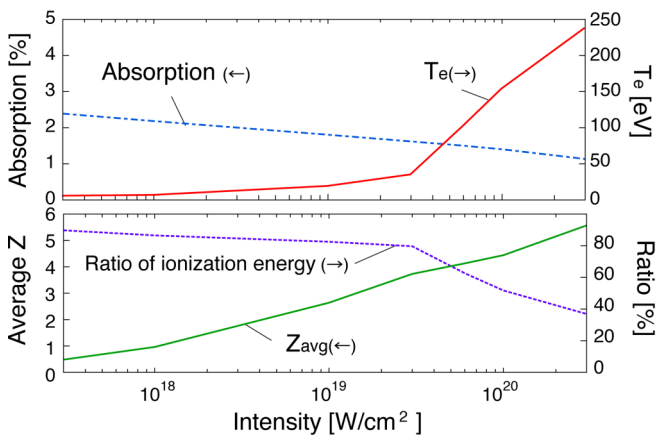

FIG. 2. (Color online) Intensity dependence of the absorption, average ionization degree ($Z_{\rm avg}$), bulk temperature (T_e), and the ratio of energy used for collisional ionization to the absorbed energy. $Z_{\rm avg}$ and T_e are measured along the laser axis at 200 fs, after the x-ray laser has passed through the target completely.

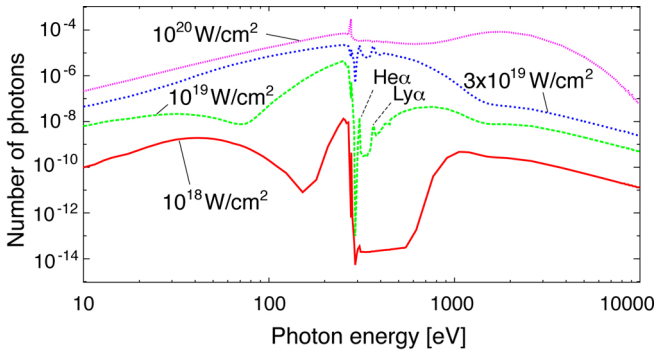

FIG. 3. (Color online) Spectrum of x-ray photons emitted backwards from the target surface integrated until $t = 200$ fs for different x-ray laser intensities: 10^{18}, 10^{19}, 3×10^{19}, and 10^{20} W/cm^2.

This is because both photoionization and electron collisional ionization become more important with higher laser energy, but the photoionization cross section decreases with further ionization.

Interestingly, the temperature increases slowly to about 20 eV up to an intensity of 3×10^{19} W/cm^2 but then rapidly climbs beyond 100 eV for higher intensities. On the contrary, the percentage of energy spent on impact ionization remains at about 80% up to 3×10^{19} W/cm^2 but then rapidly falls with higher intensities. In order to ionize carbon atoms beyond $Z_i = 4$ (He-like C), an ionization energy $I_p = 378$ eV is required to remove the tightly bound $1s^2$ inner-shell electrons—a substantial increase from $I_p \leqslant 64$ eV for the more loosely bound outer-shell electrons. At the intensity 3×10^{19} W/cm^2, the average charge state is $Z_i = 4$ and the majority of "easy" outer-shell electrons have been ionized, but there is not yet a significant population of thermal electrons with energy greater than 378 eV that is capable of ionizing the remaining inner-shell electrons, and so additional absorbed energy tends to be stored thermally instead of being spent ionizing. This is why the temperature increases rapidly and the ratio of ionization energy drops quickly beyond 3×10^{19} W/cm^2.

Figure 3 shows the emergent photon spectrum emitted backward from the target surface and integrated up to the time when the x-ray laser pulse has passed completely through the target. By increasing the laser intensity, the total number of emitted photons increases. The photon spectrum displays bound-bound transitions—one He α from the $1s^2$-$1s2p$ transition of He-like carbon (305 eV) and another Ly α from the $1s$-$2p$ transition of H-like carbon (364 eV)—observed at $I \leqslant 3 \times 10^{19}$ W/cm^2. The structure of the bound-bound emission is lost at intensities $>10^{20}$ W/cm^2 when carbon becomes almost fully ionized.

We discuss two parameters [17] of the XFEL-produced plasmas. The first is the ion-ion Coulomb coupling parameter defined as $\Gamma \equiv Z_i e^2/aT$, where $a = n_i^{-1/3}$ and T are the average interparticle spacing and thermal temperature, respectively. At the end of the simulation, 200 fs after the interaction, the electron temperature is still higher than the ion temperature. It takes several hundred additional femtoseconds to become equilibrated, i.e., for $T_i \sim T_e$. We roughly estimate the thermal equilibrium temperature by solving the energy transfer equation between electrons and ions using the energy and density obtained from the simulation. The second parameter is the

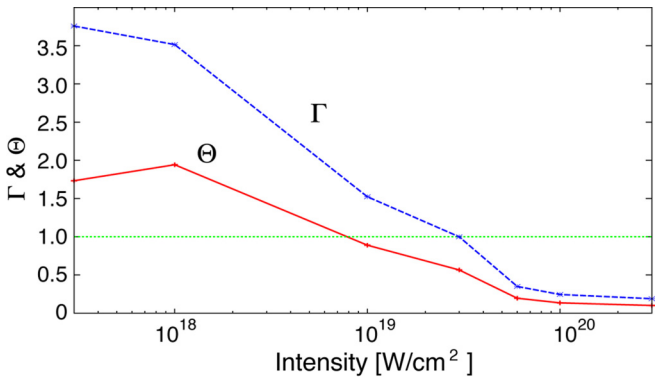

FIG. 4. (Color online) The Coulomb coupling parameter Γ (blue dashed line) and the degeneracy parameter Θ (red solid line) in the XFEL-produced plasmas.

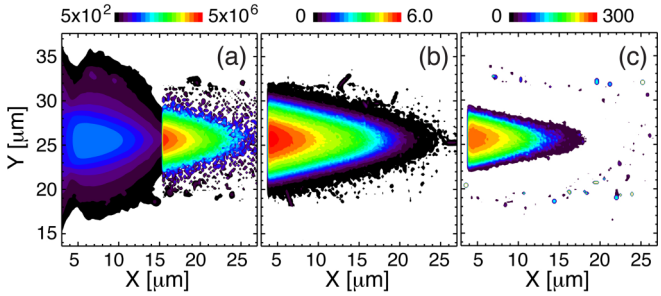

FIG. 5. (Color online) 2D PICLS simulation results of a carbon target irradiated by an x-ray laser with $I = 10^{18}$ W/cm^2 and 1 keV photon energy. The plots, observed at 110 fs as in Fig. 1, are (a) the x-ray energy density (J/cm^3) (logarithmic scale), (b) the average charge state (linear scale), and (c) the electron temperature (eV) (linear scale).

electron degeneracy parameter defined as $\Theta \equiv T_F/T_e$, where $T_F = \hbar^2(3\pi^2 n_e)^{2/3}/2m_e$ is the Fermi temperature. Figure 4 shows Γ and Θ calculated in the XFEL-produced plasmas in the central region. When the intensity $I < 10^{19}$ W/cm^2, both Γ and Θ are greater than 1. This means the plasma is strongly coupled and degenerate, i.e., in the "warm dense matter" regime. However, when $I > 3 \times 10^{19}$ W/cm^2, the plasma becomes weakly coupled, nondegenerate high energy density matter due to the nonlinear temperature increase seen in Fig. 2.

By changing the x-ray laser photon energy we can alter the heating depth, as demonstrated in Fig. 5. Since the photoionization opacity for 1 keV photons is about 5000 cm^{-1}, three orders of magnitude higher than that for 9 keV photons, a 1 keV x-ray laser would be totally absorbed and attenuated within a few microns. Figure 5(a) shows that the 1 keV x-ray laser penetrates more than 15 μm—much deeper than estimated using the cold opacity. X rays are emitted from the hot plasma created behind the laser pulse where the target becomes fully ionized and a bulk electron temperature of 300 eV is achieved, as seen in Figs. 5(b) and 5(c). What is happening here is an induced transparency of the plasma to the x-ray laser as the ionization proceeds. Since the photoionization opacity is extremely high, the x-ray laser is mostly absorbed until the initial penetration depth of the carbon atoms is highly ionized, after which time the photoionization cross section decreases and the laser can proceed to interact with deeper regions in the target.

We have developed a simulation tool that solves the radiation transport in the particle-in-cell code self-consistently and studied x-ray laser-matter interactions at 9 keV, including kinetic effects. Photoionization is the dominant absorption mechanism for low-Z matter such as carbon graphite at this photon energy. The bulk electron temperature in solid graphite increases nonlinearly with increasing x-ray laser intensity due to the ionization potential gap from $Z_i = 4$ to 5. The heated volume and temperature are tunable by changing the x-ray laser energy and photon energy, which is attractive for various applications. In high-Z materials such as copper, other absorption processes besides photoionization also become important. These results will be reported in a forthcoming publication.

This work was supported by DOE/OFES under Contract No. DE-SC0008827.

[1] Department of Energy, SLAC National Accelerator Laboratory Report No. SLAC-R-1007, 2013 (unpublished).
[2] H. Yumoto, H. Miura, T. Koyama *et al.*, Nat. Photonics **7**, 43 (2013).
[3] M. Nakatsutsumi and T. Tschentscher, XFEL.EU Technical Report No. XFEL.EU TN-2013-003, 2013, p. 80 (unpublished).
[4] S. Vinko *et al.*, Nature (London) **482**, 59 (2012).
[5] G. Chabrier, Plasma Phys. Controlled Fusion **51**, 124014 (2009).
[6] E. Behar, M. Sako, and S. M. Kahn, Astrophys. J. **563**, 497 (2001).
[7] Y. Sentoku and A. J. Kemp, J. Comput. Phys. **227**, 6846 (2008).
[8] C. E. Lee, Los Alamos Scientific Laboratory Report No. LA-2595, 1962 (unpublished).
[9] T. Yabe *et al.*, Comput. Phys. Commun. **66**, 233 (1991).
[10] H.-K. Chung, M. H. Chen, W. L. Morgan, Y. Ralchenko, and R. W. Lee, High Energy Density Phys. **1**, 3 (2005).
[11] H. A. Kramers, Philos. Mag. **46**, 836 (1923).
[12] B. L. Henke, E. M. Gullikson, and J. C. Davis, At. Data Nucl. Data Tables **54**, 181 (1993).
[13] R. Mishra, P. Leblanc, Y. Sentoku *et al.*, Phys. Plasmas **20**, 072704 (2013).
[14] O. Hemmers, R. Guillemin, and D. W. Lindle, Radiat. Phys. Chem. **70**, 123 (2004).
[15] L. Spitzer, Jr., *Physics of Fully Ionized Gases* (Interscience, New York, 1956), Chap. 5.
[16] National Institute of Standards and Technology, ESTAR database, http://physics.nist.gov/PhysRefData/Star/Text/method.html.
[17] M. S. Murillo, Phys. Plasmas **11**, 2964 (2004).